HHS Public Access

Author manuscript

Cell Rep. Author manuscript; available in PMC 2019 August 14.

Published in final edited form as:

Cell Rep. 2019 July 30; 28(5): 1323–1334.e4. doi:10.1016/j.celrep.2019.06.093.

Metabolic Deregulation of the Blood-Outer Retinal Barrier in Retinitis Pigmentosa

Wei Wang[1,10], **Ashwini Kini**[1,10], **Yekai Wang**[5], **Tingting Liu**[1,6], **Yao Chen**[1], **Eric Vukmanic**[1], **Douglas Emery**[1], **Yongqing Liu**[1,2], **Xiaoqin Lu**[1], **Lei Jin**[1,7], **San Joon Lee**[1,8], **Patrick Scott**[1], **Xiao Liu**[1,9], **Kevin Dean**[1], **Qingxian Lu**[1], **Enzo Fortuny**[4], **Robert James**[4], **Henry J. Kaplan**[1], **Jianhai Du**[5,*], **Douglas C. Dean**[1,2,3,11,*]

[1]Department of Ophthalmology and Visual Sciences, University of Louisville Health Sciences Center, Louisville, KY 40202, USA

[2]James Graham Brown Cancer Center, University of Louisville Health Sciences Center, Louisville, KY 40202, USA

[3]Birth Defects Center, University of Louisville Health Sciences Center, Louisville, KY 40202, USA

[4]Department of Neurosurgery, University of Louisville Health Sciences Center, Louisville, KY 40202, USA

[5]Departments of Ophthalmology and Biochemistry, West Virginia University, Morgantown, WV 26506, USA

[6]The Third Affiliated Hospital of Dalian Medical University, 40 Qianshan Road, Dalian 116033, China

[7]The Affiliated Hospital of Shandong Traditional Chinese Medicine University, 48 Yingxiongshan Road, Jinan 250031, China

[8]Department of Ophthalmology, Kosin University College of Medicine, 262 Gamcheon-ro, Seo-gu, Busan 49267, Korea

[9]Department of Ophthalmology, Second Xiangya Hospital of Central South University, 139 Middle Renmin Road, Changsha 410011, China

[10]These authors contributed equally

[11]Lead Contact

*Correspondence: jianhai.du@wvumedicine.org (J.D.), douglas.dean@louisville.edu (D.C.D.).

AUTHOR CONTRIBUTIONS

W.W., A.K., Q.L., H.J.K., J.D., and D.C.D. conceived and designed experiments. W.W., A.K., Y.C., T.L., and X. Liu performed liposome injections and evaluated glucose transport. X. Lu, K.D., and Y.L. performed immunohistochemistry. A.K. and Q.L. analyzed Mertk mice and RCS rats. E.V. and D.E. performed and analyzed ERGs. W.W., Y.C., L.J., X. Liu, and W.W. performed OKRs. S.J.L. followed retinal changes during mouse RP progression. P.S. analyzed retinal histology. Y.W. and J.D. performed LC MS/MS and GS/MS on RPE and retinal tissues. R.J. and E.F. performed pig catheterizations. W.W., A.K., H.J.K., J.D., and D.C.D. analyzed results and wrote the manuscript.

DECLARATION OF INTERESTS

The authors declare no competing interests.

SUPPLEMENTAL INFORMATION

Supplemental Information can be found online at https://doi.org/10.1016/j.celrep.2019.06.093.

SUMMARY

Retinitis pigmentosa (RP) initiates with diminished rod photoreceptor function, causing peripheral and nighttime vision loss. However, subsequent loss of cone function and high-resolution daylight and color vision is most debilitating. Visual pigment-rich photoreceptor outer segments (OS) undergo phagocytosis by the retinal pigment epithelium (RPE), and the RPE also acts as a blood-outer retinal barrier transporting nutrients, including glucose, to photoreceptors. We provide evidence that contact between externalized phosphatidylserine (PS) on OS tips and apical RPE receptors activates Akt, linking phagocytosis with glucose transport to photoreceptors for new OS synthesis. As abundant mutant rod OS tips shorten in RP, Akt activation is lost, and onset of glucose metabolism in the RPE and diminished glucose transport combine to cause photoreceptor starvation and accompanying retinal metabolome changes. Subretinal injection of OS tip mimetics displaying PS restores Akt activation, glucose transport, and cone function in end-stage RP after rods are lost.

In Brief

Wang et al. show that onset of glucose metabolism in the retinal pigment epithelium (RPE), which acts as the blood-outer retinal barrier, and inhibition of RPE glucose transport to photoreceptors combine to cause photoreceptor starvation and vision loss in retinitis pigmentosa.

Graphical Abstract

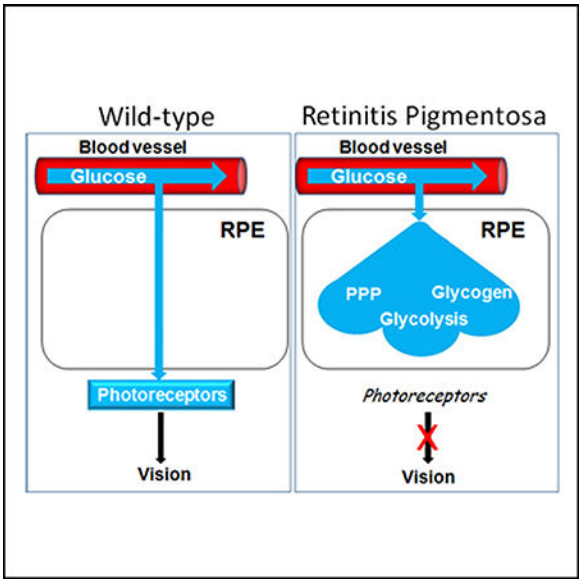

INTRODUCTION

Retinitis pigmentosa (RP) most frequently initiates with loss of rod photoreceptor-dependent peripheral vision and dark adaptation (Fahim et al., 1993). At least 200 different mutations in more than 60 genes are linked to RP. Many of these mutations arise in genes expressed specifically in rods and their pathways vary dramatically ranging from visual pigments and visual cycle to metabolism and RNA splicing. Some mutations arise in the retinal pigment

epithelium (RPE), where phagocytosis of photoreceptor protein- and fatty acid-rich outer segments (OS) that house visual pigment occurs, and that act as a blood-outer retinal barrier supplying nutrients from the choroidal circulation to adjacent photoreceptors for new OS synthesis. Despite this diversity of mutations in different cell types, RP in patients is highlighted by gradual, progressive loss of rod function, and ultimately rod death. Further complicating RP, cones then start to lose their function (Aït-Ali et al., 2015; Chinchore et al., 2017; Petit et al., 2018; Wang et al., 2016), which is critical for high-resolution daylight and color vision utilized for reading, driving, facial recognition, and other daily tasks. This secondary loss of cone function is a focus of ongoing investigations.

New OS synthesis to replace shed tips is a major metabolic commitment in photoreceptors. There is mounting evidence that loss of cone function in RP is linked to glycolytic failure (Léveillard et al., 2019; Park et al., 2018). As with other neurons, photoreceptors depend upon glucose, and blocking glycolysis in cones *in vivo* by inhibition of glyceraldehyde 3-phosphate dehydrogenase led to rapid loss of OS synthesis and function (Wang et al., 2011a). Glucose in the choroidal circulation is transported through the RPE to photoreceptors via Glut1 transporters on the surface of the cells (Swarup et al., 2019), and in cones, it activates the glucose-dependent Mondo family of transcription factors to induce genes directing glucose metabolism (Havula and Hietakangas, 2018; Wang et al., 2016). Consistent with diminished glucose transport to cones, glucose-dependent genes are downregulated in the cells as RP progresses (Wang et al., 2016). Increasing glucose availability to—and uptake into—cones by direct subretinal injection of glucose or early viral expression of rod-derived cone viability factor (Rdcvf; which promotes glucose uptake into cones), delayed their loss of function during RP progression (Aït-Ali et al., 2015; Byrne et al., 2015; Punzo et al., 2009; Venkatesh et al., 2015; Wang et al., 2016). Consistently, studies aimed at enhancing glycolysis in photoreceptors by mutation/inhibition of the glycolytic repressor, Sirt6, likewise delayed loss of photoreceptor function in RP (Zhang et al., 2016), and activation of mTorc1 in cones, which drives glucose transport and metabolism, via insulin or *Pten* mutation also prolonged cone function in RP (Punzo et al., 2009; Venkatesh et al., 2015). Together, these results suggest glucose starvation is blocking new OS synthesis and function in cone photoreceptors as RP progresses, but how this starvation might be linked to the glucose-demanding OS phagocytosis/renewal cycle *in vivo* is still unclear.

Phosphatidylserine (PS) is externalized on dying cells, where it marks the cells for phagocytosis by macrophages (Birge et al., 2016). Similarly, PS is externalized on extending OS tips, where it forms complexes with integrins and Tam family receptors on the RPE apical surface (Ruggiero et al., 2012). Resulting crosssignaling between these receptors leads to activating phosphorylation of Akt (pAkt), which drives cytoskeletal reorganization required for RPE OS phagocytosis (Chiang et al., 2017). pAkt also classically induces glucose transport, raising the possibility that glucose transport through the RPE to photoreceptors might be linked to OS tip phagocytosis. Via pAkt, insulin not only releases the glucose transporter, Glut4, sequestered in the cytoplasm, it also inhibits Glut family endocytosis, and together, these pAkt activities increase cell surface expression of Glut family members (Beg et al., 2017; Mackenzie and Elliott, 2014). At the molecular level, Glut4, as well as Glut1, binds to the α-arrestin, Txnip, which is phosphorylated by pAkt

causing its degradation (Waldhart et al., 2017; Wu et al., 2013). α-arrestins, which are related to β-arrestins and visual arrestins, act as scaffolds recruiting receptors into clathrin-coated pits for endocytosis via their interaction with clathrin-bound adaptor proteins (Moaven et al., 2013; Nelson et al., 2008). Txnip bridges Glut1/Glut4 to a clathrin-adaptor protein 2 (AP2) complex, which is enriched on the apical surface of polarized epithelial cells where it enforces cell polarity by selective protein endocytosis (Lin et al., 2015; Waldhart et al., 2017; Wu et al., 2013). *Txnip* is glucose-inducible, and it provides negative feedback to trigger Glut family endocytosis that classically regulates insulin-dependent and -independent glucose transport; *Txnip* mutation or degradation in response to pAkt leads to deregulated glucose transport and hypoglycemia (Chutkow et al., 2008). As the level of Txnip rises with diminishing pAkt, it feeds back to further inhibit Akt activation (Huy et al., 2018).

At the onset of rod OS (ROS) shortening in RP, we show pAkt diminishes, Txnip is induced, apical Glut1 is lost, and RPE glucose transport to photoreceptors is compromised. Using models of RP in mouse and pig, in the latter species cones are concentrated in a visual streak, we show subretinal injection of OS tip mimetics displaying PS activates this pAkt/Txnip/Glut1 pathway, thereby linking glucose transport to OS tip phagocytosis. Reactivation of RPE glucose transport can restore cone OS (COS) synthesis and function in end-stage RP after rods are lost. We found that glucose metabolism is inhibited in the RPE *in vivo*, preserving the flow of glucose through the RPE to photoreceptors. However, glucose metabolism, reflected by glycolysis as well as diversion of the glycolytic pathway into glycogen synthesis and the pentose phosphate pathway (PPP), was initiated in the RPE in RP. We propose that onset of glucose metabolism in the RPE combines with restricted transport to diminished glucose available to photoreceptors in RP.

RESULTS

Failure in RPE Glucose Transport to Photoreceptors in RP

To begin examining the effect of an RP mutation on glucose transport from the RPE to the photoreceptors, we utilized mice with a dominant-acting P23H *Rho* mutation knocked into one allele (Sakami et al., 2011). These RP mice lack Rd1/Rd8 mutations and were further backcrossed in the laboratory for five generations into the C57BL6 background. At postnatal day 25 (P25), the number of outer nuclear layer (ONL) rows containing photoreceptor nuclei was similar in wild type (WT) and RP mouse littermates, and likewise, rod and COS functional structures (denoted by immunostaining for Rho and cone opsin) were still similar (Figures 1A, 1B, and S1A; results not shown). However, by P35, abundant mutant ROS tips had begun to shorten in RP mice, but the number of ONL rows (~95% of cells in the ONL in mice are rods) had not decreased (Figures 1A, 1B, and S1A).

Fluorescently labeled 2-deoxyglucose was injected into the tail vein of RP and WT mouse littermates, and uptake into RPE and retina was examined in tissue sections extending ~1 mm from the optic nerve 1 h later, as we described (Wang et al., 2016). At P25, before onset of mutant ROS shortening, both RP and WT littermates showed similar “glucose” uptake into photoreceptor inner segments (IS), and little glucose was retained in the RPE (Figures 1C and 1D). Notably, most glucose was evident in the outer retina under these conditions.

With onset of ROS shortening at P35 in RP, glucose accumulated in the RPE and it diminished in photoreceptors (Figures 1E–1F′; also see Figure 3 below).

Next, we used liquid chromatography/mass spectrometry (LC/MS) to quantify steady-state levels of glucose in the RPE and retina in WT versus RP mice. Consistent with the fluorescence experiments above, we found glucose was increased in the RPE and diminished in the retina of RP mice (Figure 1G).

These results provide two lines of evidence glucose becomes sequestered in the RPE, diminishing its transport to photoreceptors as RP progresses. Onset of glucose retention in the RPE coincides with initial shortening of abundant mutant ROS tips, which normally contact the RPE to initiate phagocytosis. Notably, because the number of mutant rods has not diminished at P35 (Figure 1A), both rods and cones are starved for glucose at this age in RP mice.

Glut1 Is Diminished on the RPE in RP

Glut1 is critical for glucose transport from the choroid circulation into the RPE and subsequent transport out of the RPE to photoreceptors (Swarup et al., 2019). As shown previously, we found Glut1 was expressed on both the basal and apical surfaces of the RPE in WT mice, and it was evident on photoreceptor IS (Figures 1H, 1H′, and S1B). A similar pattern of Glut1 was seen at P25 in RP mice, but by P35 Glut1 had diminished on the apical RPE surface in RP mice (Figures 1I–1I′′), providing an explanation for failure to transport glucose apically out of the RPE to photoreceptors at this age. Western blotting for Glut1 at P40 showed that its level in the RPE is similar in WT and RP littermates (Figure 2A), demonstrating that loss of apical expression in RP is not linked to an overall decrease in the level of Glut1 in the RPE. In this regard, Glut1 in endocytic vesicles is recycled to the cell surface without a requirement for new Glut1 synthesis (Waldhart et al., 2017). As noted above, a Glut1-Txnip complex tethered to clathrin-coated pits via interaction with apically localized AP-2 drives endocytosis of Glut1.

Loss of pAkt in the RPE in RP

pAkt accumulates in the RPE during phagocytosis, where it drives phosphorylation of proteins important for cytoskeletal changes critical for phagocytosis, and accordingly, inhibition of pAkt blocks RPE phagocytosis of OS (Chiang et al., 2017). Consistent with diminished phagocytosis as mutant ROS begin to shorten in RP mice, we found that pAkt decreased in the RPE (Figures 2A–2C).

Txnip Increases with Loss of pAkt in the RPE in RP

As noted above, Tnxip classically drives endocytosis of Glut family members in a feedback pathway to restrict glucose transport. In response to insulin and other Akt activating pathways, pAkt phosphorylates Txnip causing its degradation, thereby increasing the level of Glut family members on the cell surface (Waldhart et al., 2017). Consistent with loss of pAkt, Txnip increased in the RPE in RP (Figures 2D and 2E). Txnip is the most glucose-inducible gene identified, and with diminished glucose transport to photoreceptor inner segments (IS) in RP, Txnip expression diminished in the IS (Figures 2D and 2E).

Mertk Is Required for Apical Glut1 Expression and Glucose Transport from the RPE to Photoreceptors in Rats

Signaling between integrins and the Tam family member Mertk on the RPE in response to PS on OS tips is critical for phagocytosis, and cleaved, soluble Mertk released from the RPE acts as a feedback decoy to limit the duration of phagocytosis (Law et al., 2015; Ruggiero et al., 2012). Mutation of *Mertk* in RCS rats leads to an RP phenotype, despite this mutation arising in a gene expressed in the RPE as opposed to rods. As in P23H *Rho* RP mice, fluorescent 2-deoxyglucose was sequestered in the RPE and not transported to photoreceptors in RCS rats (Figures 2F, 2G, and S2). Likewise, Glut1 was present on the basal surface of the RPE in RCS rats, but it was diminished on the apical surface of the cells at P30 (Figures 2H and 2I). These findings provide evidence that Mertk is required for apical expression of Glut1 on the RPE in rats, and thus for transport of glucose from the RPE to photoreceptors. As a control, Mertk was maintained on the apical surface of the RPE in RP mice at P40 (Figure S3A), suggesting failure in Mertk signaling in RP is not due to loss of the protein. Instead, we hypothesized loss of Mertk signaling in RP is due to failure of the receptor to form an activation complex with PS as mutant ROS begin to shorten (Lemke, 2017). Notably, the closely related Tam family member Tyro3, which also forms a signaling complex with PS (Meyer et al., 2015), is expressed along with Mertk in C57BL6 mice, causing *Mertk* mutation alone to have less of an impact on RPE in this strain (Vollrath et al., 2015). Notably, PS complex formation with Mertk signals pAkt formation (Lemke, 2017).

PS-Displaying OS Tip Mimetics Restore RPE Apical Glut1 and Glucose Transport in RP

In an effort to demonstrate PS on OS tips is responsible for regulating RPE apical Glut1 and glucose transport, we subretinally injected PS-containing liposomes, as OS tip mimetics, into RP mice at P60, after apical Glut1 and glucose transport from the RPE to photoreceptors was inhibited. Approximately 3,000 DiIlabeled unilamellar PS liposomes (~1 μm in diameter) (Figure 3A) containing equal molar amounts of PS and phosphatidylcholine (PC) in 2 μL were injected. PS liposome presence in the subretinal space decreased in a gradient from the injection site (Figures 3A and S3B). Glut1 expression was re-established on the apical surface of the RPE in the region surrounding the injection site at day three (Figure 3B), and pAkt was restored (Figure S4A). Accordingly, glucose transport from the RPE to photoreceptors was restored in an ~300 μm region on either side of the injection site, coinciding with this gradient of PS liposomes (Figures 3C–3E). Glucose remained sequestered in the RPE in RP mice receiving control injections with PC-only liposomes (Figure 3F). Notably, PS liposome injection failed to restore glucose transport in RCS rats.

Transient Restoration of Photoreceptor OS and Function following PS Liposome Injection

We hypothesized loss of COS synthesis is due to progressive deprivation of glucose that initiates at P35 in P23H *Rho* RP mice, and PS liposome-mediated restoration of glucose transport to photoreceptors would restore OS synthesis and function. By P60, COS had diminished and cone opsin was reduced but still evident in cone inner segments. At this age, opsin^{+} COS were restored surrounding the PS liposome injection site at day 3 (Figures 4G, 4G′, and 4I).

Above, we demonstrated that rods are also deprived of glucose as their OS begin to shorten early in RP mice (Figures 1A–1F′). These findings raised the question as to whether this glucose starvation is contributing to or accelerating loss of mutant ROS and function in RP. We then investigated whether Rho^+ ROS and function might be restored in RP mice after PS liposome injection. ROS had diminished at P60, but ONL rows had only decreased by ~40% at this age, indicating many rod cell bodies were still present (Figure S7). As with COS, we found that Rho^+ ROS were restored in a similar region surrounding PS liposome injection sites (Figures 3H and 3I). These results provide evidence that glucose starvation is contributing to loss of ROS in RP mice, even though the initiating RP mutation is in the OS pigment gene *Rho*.

Visual acuity, measured by optokinetic response (OKR) under photopic conditions, was diminished by P40 in RP mice (Figure 4A). We then asked if the increase in COS we observed following PS liposome injection was sufficient to improve visual acuity. Indeed, visual acuity was improved 3 days after PS liposome injection, but, as a control, liposomes containing only PC failed to restore visual acuity (Figure 4A). These results provide evidence of a functional role for PS in the liposomes.

As a second measure of photoreceptor function, electroretinograms (ERGs) were performed in RP mice following injection with PS liposomes. These experiments were in older mice at P117, where ONL rows had diminished to ~50% (Figure S4B). The ERG under both photopic and scotopic conditions was improved following PS liposome injection (Figures 4B–4C′), providing evidence both rod and cone function can be significantly restored by OS tip mimetics that reactivate glucose transport to photoreceptors in RP.

PS Liposomes Can Restore COS Synthesis and Function in End-Stage RP in Pigs

Next, we moved experiments to a large animal model of RP, P23H *RHO* pigs (Ross et al., 2012; Wang et al., 2016), where cones are concentrated in a visual streak. In these pigs, ROS are diminished by P30, and all rod cell bodies are lost by P120 (Figures 5A–5C′ and S5) (Wang et al., 2016). COS length begins to diminish at P30, and all COS are lost by P120. In contrast to rods, cone nuclei persist at P120, and cone IS are still evident at this age, but their structure is partially disrupted (Figures 5C and 5C′). Their endoplasmic reticulum (ER) and golgi have migrated from their normal position in the IS adjacent to the mitochondria-rich ellipsoid to a perinuclear position on the inner side of the outer limiting membrane (OLM). The cilium connecting IS and OS is lost, with only remnants persisting on some cones. Previously, we found that cones displaying this morphology at P120 did not die and persisted for more than 6 years in these pigs (Wang et al., 2016). Thus, P120 reflects end-stage disease where all rods are lost, and the ONL consists of several rows of cones lacking OS (Figure 5C′). Previously, we found that transplant of WT rods into RP pigs all the way out to 18 months of age was able to restore COS and function, demonstrating that these dormant cones can be reactivated in a rod-dependent fashion (Wang et al., 2016). Based on our findings above with mice, we hypothesized PS on transplanted ROS tips in these experiments was contacting the RPE to re-establish glucose transport to endogenous cones. Consistent with this possibility, glucose-responsive genes were re-induced, and subretinal

injection of glucose at this age likewise restored dormant COS synthesis and function (Wang et al., 2016).

We injected 50 μL of Dil-labeled PS liposomes, at a concentration of 1,500 liposomes per μL, subretinally into the cone-rich visual streak of RP pigs at P120, and control injections were performed in the contralateral eye. Photopic multifocal (mf)ERG was used to assess electrophysiology at sites of injection, as we have described (Wang et al., 2016). Fields were divided into 241 hexagons; color maps depicting the n1-p1 wavelet height in each hexagon, along with the wavelets themselves, are shown in Figure 6A. Wavelets in the region of the bleb resulting from PS liposome injection in the visual streak, outlined by dashed lines, were averaged (Figure 6B). As we reported previously (Wang et al., 2016), baseline mfERG prior to injection was diminished at P120 in RP pigs compared to WT littermates, and PS liposomes restored mfERG in the RP animals to near WT levels (Figures 6A and 6B). Notably, this recovery of mfERG was similar to that observed three days following direct subretinal injection of glucose (Wang et al., 2016). Consistent with restoration of mfERG, cone IS and COS on the RPE were restored surrounding injection sites (Figures 6C–6J, S6, S7, and S12).

Taken together, our results suggest that externalized PS on abundant ROS tips complexing with receptors on the RPE is responsible for initiating glucose transport from the RPE to photoreceptors for new OS synthesis. These complementary results in the pig extend this pathway to a large animal model where cones are concentrated in a visual streak, and they show that re-engagement of the PS component of OS with the RPE is sufficient to restore glucose transport and function to cones in end-stage RP after rods are lost.

Onset of Glucose Metabolism in the RPE in RP

Next, we isolated RPE from WT and RP mice for steady-state LC/MS analysis. Mice at P60 were used for these assays. RPE was rapidly separated from Bruch's membrane and choroid (within 5 min of eye removal) using a combination of dispase and mechanical dissection/scraping with a modified Pasteur pipette with a curved end. We obtained 5,000–6,000 cells per eye with this technique. RPE from a single eye was sufficient for at least four repeat analyses. Intermediates in glucose metabolism were either low or undetectable in the RPE from WT mice, but these intermediates accumulated in the RPE in RP (Figure 7A). Beyond glycolysis, the glycolytic pathway at the point of glucose-6-phosphate (G6P) can be diverted into the NADPH-generating pentose phosphate pathway (PPP). Consistent with activation of PPP in RPE from RP mice, PPP intermediates ribulose-5-phosphate and erythose-4-phosphate, along with NADPH, were increased (Figure 7A). Further, G6P can be metabolized to glycogen for glucose storage. Consistent with onset of the glycogen synthesis pathway in RPE from RP mice, glucose-1-phosphate, UDP-glucose, and UDP were elevated in the cells (Figure 7A). These results provide evidence that glucose metabolism including glycolysis, PPP, and glycogen synthesis is activated in the RPE during RP. We propose that reduced glucose metabolism in the RPE allows its flow-through to photoreceptors, but onset of RPE glucose metabolism combines with diminished transport to reduce glucose available to photoreceptors in RP (Figure 7F).

Despite a lack of evident glycolysis in the RPE, lactate was present in the cells (Figure 7A). Lactate can be generated from glucose in the retina (Figure 7D), thus it is likely lactate from the retina is being transported to the RPE. It has been reported that RPE in culture can metabolize lactate (Kanow et al., 2017), thus we hypothesized that RPE might be metabolizing lactate in place of glucose. We injected 13C lactate and analyzed its metabolism 45 min later. Although 13C lactate was taken up from the choroidal circulation by the RPE, little metabolism to pyruvate was evident under these conditions (Figure 7B), suggesting limited metabolism of lactate accumulating in the RPE *in vivo*. By contrast, 13C from lactate was incorporated into pyruvate and citrate in the retina (Figure 7B), demonstrating that the retina can metabolize lactate.

In an attempt to follow uptake into and secretion of metabolites such as lactate by the RPE, we catheterized the pig ophthalmic artery entering the arterial circulation via the femoral artery and inserted a femoral microcatheter into the ophthalmic artery at the branch point of the main ciliary artery, which supplies the choroid (Figure S8). Serum samples were taken at this site upstream of the RPE from the ciliary artery and downstream of the RPE from the vortex vein (that drains the choroid) in WT and RP littermates at P90. Steady-state levels of metabolites in serum were then analyzed via LC/MS, as described (Grenell et al., 2019; Zhang et al., 2016). Peak intensity ratios for 89 different peaks were assessed, and principal component analysis suggests that, as expected, many differences are driven by changes in vortex vein samples downstream of the RPE in WT versus RP pigs (Figures S9, S10, and S11), consistent with differences in secretion and uptake by the RPE in RP. Notably, we found that lactate was increased in vortex vein samples compared to ciliary artery samples (Figures 7C and S11), providing evidence that lactate accumulating in the RPE is being secreted into the choroid circulation.

Even though glucose metabolism was diminished in the RPE in WT animals, TCA cycle intermediates were nevertheless present (Figure 7A). Our results above suggest that lactate is not a major source of these TCA cycle intermediates. Another possible source of the intermediates is fatty acid oxidation (FAO) following OS tip phagocytosis. Indeed, RPE in culture have been shown to oxidize palmitate, which comprises ~15% of OS fatty acids, into acetyl CoA for entry into the TCA cycle (Du et al., 2016a). We then injected 13C palmitate into WT and RP mice, but we did not observe differences in 13C incorporation into the TCA cycle in the RPE (results not shown). These results likely mean that palmitate provided via the circulation can be metabolized in a similar fashion by RPE in WT and RP mice, and the difference in RP is that RPE no longer have access to high levels of fatty acids as OS phagocytosis diminishes. In this regard, the most notable difference in secretion from the RPE in WT versus RP pigs is a >10-fold increase in acetyl carnitine secretion in WT (Figure 7C). Acetyl carnitine serves as a sink for excess acetyl CoA arising from FAO, and it feeds back to block PDH activity and thereby prevent acetyl CoA generation from pyruvate, derived from either glycolysis or generation from lactate via LDH (Hue and Taegtmeyer, 2009). Moreover, FAO blocks glycolysis at several additional steps (e.g., the Randell cycle) (Hue and Taegtmeyer, 2009). Acetyl carnitine generation is critical in buffering high acetyl CoA levels derived from FAO (Longo et al., 2016). We suggest that FAO is blocking glycolysis in the RPE, and acetyl carnitine secretion reflects buffering of excess acetyl CoA from FAO.

Diminished Retinal 13C Glucose Metabolism in RP

13C glucose (40%) in 2 mL was infused via a microcatheter in the ciliary artery upstream of the RPE in WT and RP pig littermates at P90 over the course of 30 min. The retina was analyzed by GC/MS for 13C incorporation into metabolic pools. We observed diminished 13C incorporation in aerobic glycolysis and TCA cycle intermediates in RP pigs (Figures 7D and 7E), suggesting glucose metabolism is contributing less to these metabolic pools as rods are lost in the RP retina.

A Low-Energy Environment in WT RPE Is Reversed in RP

Consistent with a high-energy requirement for ongoing OS phagocytosis, ATP was low in RPE from WT animals compared to RP (Figure 7A). ATP can be converted reversibly to phosphocreatine, which serves as a high-energy reservoir. In macrophages, a phosphocreatine reservoir drives ATP generation locally at sites of cytoskeletal assembly during phagocytosis (Kuiper et al., 2008). Like ATP, phosphocreatine levels were low in RPE from WT mice compared to RP littermates. This increase in energy in RPE from RP mice is consistent with diminished energy-demanding phagocytosis.

Elevated Alpha-Ketoglutarate (α-KG) in the RPE in RP

Although other TCA cycle intermediates were similar, steady-state levels of α-KG (also known as 2-oxoglutarate) were dramatically elevated in the RPE from RP mice (Figure 7A). Previously, Du et al. (2016b) demonstrated that glutamine is metabolized to yield a high level of α-KG in cultured RPE cells, and a portion of this α-KG is utilized for reductive carboxylation in reversal of the TCA cycle to generate citrate. α-KG/2-oxoglutarate is an obligatory co-substrate for 2-oxoglutarate-dependent dioxygenases including TET family members that hydroxymethylate DNA (leading ultimately to methylation), the KDM family of histone demethylases, and prolyl hydroxylases that regulate hypoxia inducible Hif1a, which itself is a major metabolic regulator (Berry and Janknecht, 2013; Chin et al., 2014; Rasmussen and Helin, 2016). By contrast, the TCA intermediate succinate, which is downstream of α-KG in the normal turning of the cycle, competes with α-KG to inhibit these epigenetic enzymes. Thus, the ratio of α-KG-to-succinate controls epigenetic reprogramming, and the high α-KG-to-succinate ratio in the RPE in RP demonstrates an excess of α-KG, beyond what might be utilized for citrate production. These findings raise the interesting possibility that the RPE might undergo epigenetic reprogramming as RP progresses.

DISCUSSION

RP is a genetically diverse disease linked to mutations in more than 60 genes. Although some mutations target the visual pigment Rho, structural components of OS that house Rho in rods and the visual cycle, many mutations are in other pathways including metabolism and RNA splicing. Some mutations, such as *Mertk*, target the RPE. How can mutations in such a wide variety of pathways and in different cells commonly give rise to a gradual loss of rod function in RP? In rods, we propose RP mutations target synthesis of functional OS, either directly via mutation of *Rho* or OS structural components, or indirectly through pathways whose inhibition contributes to general metabolic stress such that rods are unable

to sustain the high level of synthesis required to maintain OS, which becomes evident over time in gradual OS shortening as RP progresses. Our findings suggest eventual failure of shortening ROS to engage the RPE leads to disruption of glucose transport, causing photoreceptor starvation in RP (Figure 7F). Previously, we found that a block in glycolysis in rods leads to loss of OS, function, and cell death (Wang et al., 2011a). Consistent with the notion that glycolytic failure is accelerating loss of mutant rod function in RP, mutation/inhibition of the glycolytic repressor, Sirt6, in rods to enhance rod glycolysis, delayed loss of mutant ROS and function in RP (Zhang et al., 2016). We suggest that RP mutations, such as *Mertk* in the RPE, contribute to photoreceptor starvation by compromising glucose transport. Although a block in cone glycolysis also causes loss of OS and function, these cells do not die and persist in a dormant state, and their OS synthesis and function is restored once the glycolytic block diminishes (Wang et al., 2011a). We then propose that glucose starvation accelerates loss of both ROS and COS synthesis and function in RP, with rod viability being further impacted by the gene mutation responsible for RP. In end-stage RP in the pig, we show that restoration of glucose transport to persisting cones can restore OS synthesis and function in the absence of rods.

We found that glucose metabolism is diminished in the RPE *in vivo* and suggest this allows flow of unmetabolized glucose through the RPE to photoreceptors. However, glucose metabolism was initiated in the RPE in RP, which is reflected in onset of glycolysis as well as diversion of the glycolytic pathway into glycogen synthesis and the PPP. We propose that this onset of glucose metabolism combines with its restricted transport to diminish glucose available to photoreceptors in RP (Figure 7F).

Akt signaling appears to be a nexus linking OS phagocytosis to glucose transport to photoreceptors for new OS synthesis (Figure 7F). Akt can be phosphorylated on S473 or T308, and it is pAktS473 that drives cytoskeletal changes required for RPE phagocytosis of OS (Chiang et al., 2017). pAktS473 is also critical for inhibiting Glut family endocytosis and thus, promoting glucose transport (Beg et al., 2017). Notably, we also observed pAktS473 in the RPE. Txnip drives Glut1 endocytosis, and its targeting by pAkt promotes glucose transport. A complex between PS on OS tips with integrins and Tam receptors on the RPE apical surface leads to pAkt. Likewise, integrin binding to extracellular matrix ligands also triggers pAkt (Hu and Luo, 2013). A recent study found that changes in extracellular matrix composition were transmitted via integrins into the cell to regulate Txnip and, in turn, glucose transport in the cells (Sullivan et al., 2018). Notably, integrins on the RPE basal surface anchor the cell via interaction with extracellular matrix components of Bruch's membrane (Benedicto et al., 2017). As noted, α-KG is an essential co-factor for 2-oxoglutarate-dependent dioxygenases that regulate epigenetic reprogramming of cells (Berry and Janknecht, 2013; Chin et al., 2014; Rasmussen and Helin, 2016). We show elevated α-KG in the RPE in RP. However, 2-oxoglutarate-dependent dioxygenases (e.g., prolyl hydroxylases) also dictate collagen type expression and functional crosslinking, thereby altering the cell's extracellular matrix composition (Jiang et al., 2016; Smith and Talbot, 2010). In a potential feedback loop, cell adhesion via integrins also regulates α-KG to alter extracellular matrix composition (Jiang et al., 2016). Because changes in Bruch's membrane composition highlight age-related macular degeneration (AMD), it is interesting to speculate

that reciprocal signaling between the RPE basal surface and an altered Burch's membrane might de-regulate glucose transport in AMD.

Limitations of Our Study

Our results highlight RPE metabolome changes and glucose transport defects in several RP models (*Rho* mutant mice and pigs and RCS rats). It will be important to extend these findings to other RP mutations. Subretinal injection of PS-displaying OS tip mimetics was able to restore COS and function in end-stage RP, providing evidence that contact of OS tips with the RPE is linking OS phagocytosis to RPE glucose transport. However, subretinal liposome injection is not a viable long-term therapeutic option for RP patients. Characterization of the glucose metabolic and transport regulatory pathways initiated in RP highlights drugs targeting these pathways that are being evaluated in clinical trials for various cancers. Our findings showing initiation of RPE glucose metabolism and diminished glucose transport from the RPE to photoreceptors in RP provides an alternate explanation for onset of glucose starvation in photoreceptors in this disease. However, this model can synergize with previous potential therapies such as activation of mTorc1 and expression of Rdcvf to drive diminishing levels of glucose into cones as RP progresses and inhibition of Sirt6 to enhance glycolysis in photoreceptors as available glucose decreases.

STAR★METHODS

LEAD CONTACT AND MATERIALS AVAILABILITY

Further information and requests for resources and reagents should be directed to and will be fulfilled by the Lead Contact Douglas Dean (douglas.dean@louisville.edu). This study did not generate unique reagents.

EXPERIMENTAL MODEL AND SUBJECT DETAILS

Experimental design—WT and RP mice and pigs were followed for glucose transport, glucose transport pathway, metabolic changes with LC/MS and GC/MS, and histology and immunostaining for loss of photoreceptor functional structures and photoreceptor number. Electrophysiology was followed by ERG and visual acuity by OKR. Glucose transport from the RPE to photoreceptors in mice was followed by injection of fluorescent 2-deoxyglucose into the tail vein and analyzing frozen sections including the RPE and retina after one hr, and by LC/MS of the tissues. PS liposomes, as OS mimetics, were injected into the subretinal space of RP mice and into the visual streak of pigs, and glucose transport, photoreceptor OS, ERG and OKR was analyzed. Ages of animals are shown on figures or provided in legends.

Randomization—Littermates were divided into WT and RP groups for experiments. We did not detect differences in female versus male RP mice or pigs in measurements described above, thus males and females were randomly included into the study groups.

Mice and pigs: All methods were approved by the University of Louisville Institutional Animal Care and Use Committee and adhered to the ARVO Statement for Use of Animals in Ophthalmic and Vision Research. WT and P23H *Rho* mutant pig (Ross et al., 2012; Wang et al., 2016) and mouse (https://www.jax.org/strain/017628) littermates were compared in the

studies. Where indicated, PS liposomes were labeled with lipophilic carbocyanine cell tracker dye Dil (ThermoFisher) as described (https://tools.thermofisher.com/content/sfs/manuals/mp00282.pdf). Different investigators performed liposome injections, electrophysiology, OKR and histological sectioning.

For liposome injections, pigs were sedated with Telzol (2.0–8.8 mg/kg) and intubated, and they were further sedated by intubated anesthesia with 1.5% to 2% isoflurane mixed with oxygen. Intravenous access was achieved by placement of a 21-gauge catheter in an ear vein. Pupils were dilated and accommodation relaxed with topical applications of 2.5% phenylephrine hydrochloride and 1% tropicamide. 50 μL of liposomes at a concentration of 1,500 liposomes per μl in PBS were injected into the superior quadrant in the region of the visual streak, as described previously (Wang et al., 2016; Zhou et al., 2011). Control liposome injections were performed in contralateral eyes. Pigs were euthanized and retinas were analyzed for histology and immunostaining as described (Wang et al., 2016; Zhou et al., 2011).

METHOD DETAILS

Unilamellar PS liposome generation—Phospholipid unilamellar vesicle formation is described in detail at https://avantilipids.com/. Briefly, phospholipid, an equal mixture of PS and PC, purchased from Avanti Polar Lipids, in chloroform was placed in a glass test tube. Chloroform was evaporated under a gentle stream of nitrogen, and then the tube was placed in a speed vac under high vacuum for one hr. Then 2.6 mL of HBS was added to the tube to yield a final concentration of 1 mM phospholipid, and it was allowed to sit for 1 hr at room temperature. The tube was then vortexed until phospholipids formed a milky uniform suspension. The suspension was then placed in a bath sonicator at room temperature until it changed from milky to near clear (only very slightly hazy). This took approximately 30 minutes. The resulting small unilamellar vesicles were stored at 4°C.

Histology and immunostaining—Frozen sections were cut at 15 μm. The slides were blocked with 4% goat serum and 0.5% Tween-20 in PBS for 1 h at room temperature before applying the primary antibody. The slides were incubated overnight at 4°C or 1 h at room temperature with primary antibodies in blocking solution. The primary antibodies used were: anti RHO (Millipore, 1:300), rabbit anti red-green opsin (OPN1LW/OPN1MW) (Millipore 1:500), chicken anti-JH492 and JH 455 anti-cone opsin (OPN1LW/OPN1MW) (gifts from Jeremy Nathans, Johns Hopkins 1:5000), Glut1 (Thermofisher 1:200). Immunostaining for Akt phosphorylated on S473 (pAkt) was described previously (Liu et al., 2014). Immunostaining for Txnip was described previously (Wang et al., 2016). The secondary antibodies were CY3 or FITC conjugated goat anti mouse antibody or goat anti rabbit antibody. Nuclei were counterstained with DAPI, and images were captured as we described (Wang et al., 2014). As negative controls, no immunostaining was evident in the absence of primary antibodies (Figure S12).

Optokinetic Reflex (OKR)—OKR was performed using the OptoMotry system (Cerebral Mechanics, Lethbridge, AB, Canada), as we have described previously (Wang et al., 2011a). Briefly, mice standing unrestrained on a central platform tracked a rotating grating with

reflexive head movement behavior. For measurement of visual acuity, animals were assessed for this tracking behavior for a few seconds; this was repeated until unambiguous tracking was observed. Spatial frequency of the grating was increased until the animal no longer responded. The highest spatial frequency the mouse could track was identified as the threshold.

ffERG in mice—Full field ERG was recorded using a UTAS ERG system with a BigShot Ganzfeld stimulator (LKC, Technologies, Inc.) after 1 hr of darkadaptation as we have described previously (Wang et al., 2011b). Mice were anesthetized using a ketamine/xylazine mixture in normal saline and the eyes dilated using a 0.625% phenylephrine solution. Contact lens electrodes (LKC Technologies, Inc.) were placed on the cornea of each eye using artificial tears. Ground and reference electrodes were placed on the tail and on the midline of the forehead, respectively. Dark-adapted responses were recorded to dim light flashes with an inter-stimulus interval of 1 s. Responses to 30 trial flashes at −60 dB were averaged. The animals were then light-adapted for 5 min and ERG responses to 30 trial flashes at 30 dB in 5 s intervals were averaged. The b-wave amplitude was measured from baseline to b-wave peak.

mfERG in pigs—DTL corneal electrodes were used to record mfERG in light-adapted pigs as we have described (Wang et al., 2016). The mfERG stimulus is positioned relative to the optic nerve head, using a fundus image that is captured within the FMS VERIS System software (Electrodiagnostic, Inc). The same software controls stimulus presentation. Responses captured within the visual streak are positioned relative to the fundus image to align them with the response spatial density profile. mfERG signals were divided into 241 hexagons. Topographic amplitude maps are generated by assigning n1-p1 response amplitudes in each hexagon a color code. For quantification, amplitudes in hexagons within the visual streak injection sites are averaged for each eye. Then, results from different treated and control eyes are averaged.

Analysis of glucose transport in mice and rats—Heterozygous P23H *Rho* knockin mice and WT littermates were injected with 150 μl of 10 uM fluorescently labeled 2-deoxy-glucose (ThermoFisher Scientific) in the tail vein. Immunofluorescence was analyzed at 15 min, 1 hr and 2 hr time points after injection, as described (Wang et al., 2016). At these times, eyes were frozen and sections were analyzed microscopically for fluorescence using optical filters designed for fluorescein. No fluorescent labeling was seen in mice following sham tail vein injections (Figure S12). Fluorescence diminished in the retina and eye muscles by two hr after injection compared to one hr, and fluorescence was yet not evident at 15 min following injection (Wang et al., 2016). So, the 1 hr time point was used for all experiments. WT and RCS rat littermates were injected in a similar fashion with 150 μl of 10 uM fluorescently labeled 2-deoxy-glucose in the tail vein.

Femoral artery catheterization—Ciliary artery catheterization is performed with pigs under general anesthesia, positioned on a radiolucent table in the fluoroscopy suite, as described in detail previously (Morén et al., 2011). Briefly, femoral artery access in the inguinal area was obtained using the modified Seldinger technique and a 5 French Stiff

Micropuncture Access Set (Cook Medical; G48008 or G35551), which was exchanged for a standard 5 Fr 10 cm length femoral sheath. A 5-Fr diagnostic angiography catheter (with a Vert, Berenstein, Simmons-2, or Cobra) was advanced over a 0.35” guidewire in retrograde fashion along the abdominal and then thoracic aorta, over the aortic arch, prior to engaging the origin of the brachiocephalic / common carotid artery. The catheter was then advanced over the guide wire into the internal carotid artery and positioned just proximal to the petrous portion of the artery. The guide wire was removed and digital subtraction angiography used to identify the ophthalmic artery on the ipsilateral side. A standard 0.014” microwire was placed within a standard 0.17” inner diameter microcatheter and the combined microcatheter/microwire system advanced under live flurosocpy with the microwire leading and accessing the ophthalmic artery origin. The microwire was then pinned in position and the microcatheter was advanced over the microwire to selectively catheterize the ophthalmic artery of interest. The microwire was removed, digital subtraction angiography used to confirm that the microcatheter tip was within the ophthalmic artery, in place for serum collection and infusion of 13C metabolites. At the conclusion of the procedure, all catheters, wires and the femoral sheath were removed and hemostasis was achieved by manual compression of the femoral puncture. Standard radiation safety procedures with optimized shielding was followed to protect researchers and staff from direct and scatter radiation.

Steady state metabolomics using LC MS/MS—Mouse and pig retinas and RPE from WT and RP animals were extracted for metabolites (Grenell et al., 2019; Kanow et al., 2017; Zhang et al., 2016). The extracts were analyzed by a Shimadzu LC Nexera X2 UHPLC coupled with a QTRAP 5500 LC MS/MS (AB Sciex). An ACQUITY UPLC UPLC BEH Amide analytic column (2.1 X 50 mm, 1.7 μm, Waters) was used for chromatographic separation. The mobile phase was (A) water with 10 mM ammonium acetate (pH 8.9) and (B) acetonitrile/water (95/5) with 10 mM ammonium acetate (pH 8.2) (All solvents were LC–MS Optima grade from Fisher Scientific). The total run time was 11 mins with a flow rate of 0.5 ml/min with an injection volume of 5 μl. The gradient elution is 95%–61% B in 6 min, 61%–44% B at 8 min, 61%–27% B at 8.2 min, and 27%–95% B at 9 min. The column was equilibrated with 95% B at the end of each run. The source and collision gas was N2. The ion source conditions in positive and negative mode were: curtain gas (CUR) = 25 psi, collision gas (CAD) = high, ion spray voltage (IS) = 3800/- 3800 V, temperature (TEM) = 500°C, ion source gas 1 (GS1) = 50 psi, and ion source gas 2 (GS2) = 40 psi. Each metabolite was tuned with standards for optimal transitions, and 13C-nicotinic acid (Toronto Research Chemicals) was used as the internal standard. The extracted MRM peaks were integrated using MultiQuant 3.0.2 software (AB Sciex), and corrected for 13C-nicotinic acid.

13C labeled metabolite analysis by GC/MS—Metabolites were derivatized by methoxymine hydrochloride followed by Ntertbutyldimethylsilyl-N-methyltrifluoroacetamide (TBDMS) as described (Grenell et al., 2019; Kanow et al., 2017; Zhang et al., 2016). An Agilent 7890B/5977B GC/MS system with an Agilent DB-5MS column (30 m × 0.25 mm × 0.25 μm film) was used for GC separation and analysis of metabolites (5). Ultra– high-purity helium was the carrier gas at a constant flow rate of 1

mL/min. One ml of sample was injected in split-less mode by the auto sampler. The temperature gradient started at 95°C with a hold time of 2 min and then increased at a rate of 10°C/min to 300°C, where it was held for 6 min. The temperatures were set as follows: inlet 250°C, transfer line 280°C, ion source 230°C, and quadrupole 150°C. Mass spectra were collected from 80–600 m/z under selective ion monitoring mode. The data was analyzed by Agilent MassHunter Quantitative Analysis Software and natural abundance was corrected by ISOCOR software.

QUANTIFICATION AND STATISTICAL ANALYSIS

Blinding—Researchers evaluating outcomes of glucose transport, ERG, OKR and photoreceptor structure and number were blinded as to whether animals had received PS liposome injection or control injection.

Sample size—Based on standard deviations derived from our previous extensive studies of ERG, OKR, ONL rows, and photoreceptor OS number in WT and RP animals, we calculated three samples would be sufficient to detect a 30% change with a confidence of 0.95 in each of these measurements. Note that all of the changes (e.g., WT versus RP and control versus treated) in ERG, OKR, ONL rows and OS number exceed 30% and n was > 3.

Data inclusion/exclusion—In pigs we only analyzed eyes where Dil-labeled PS liposomes were confirmed after injection. Without labeled liposomes as a guide, retinal sectioning could not be directed.

Replicates—Each experiment was repeated at least three time. The number of animals and eyes evaluated is shown in the figure legends. For ERGs, 30 replicates were averaged for each eye.

Significance—Significance was calculated by Student’s t test. Error bars in figures show standard deviations.

DATA AND CODE AVAILABILITY

This study did not generate/analyze any datasets/code.

Supplementary Material

Refer to Web version on PubMed Central for supplementary material.

ACKNOWLEDGMENTS

We thank Maureen McCall for valuable comments on the manuscript and Giurong Liu for histologic sections. These studies were supported by grants from the NEI, BrightFocus Foundation, and Research to Prevent Blindness.

REFERENCES

Aït-Ali N, Fridlich R, Millet-Puel G, Clérin E, Delalande F, Jaillard C, Blond F, Perrocheau L, Reichman S, Byrne LC, et al. (2015). Rod-derived cone viability factor promotes cone survival by stimulating aerobic glycolysis. Cell 161, 817–832. [PubMed: 25957687]

Beg M, Abdullah N, Thowfeik FS, Altorki NK, and McGraw TE (2017). Distinct Akt phosphorylation states are required for insulin regulated Glut4 and Glut1-mediated glucose uptake. Elife 6, e26896. [PubMed: 28589878]

Benedicto I, Lehmann GL, Ginsberg M, Nolan DJ, Bareja R, Elemento O, Salfati Z, Alam NM, Prusky GT, Llanos P, et al. (2017). Concerted regulation of retinal pigment epithelium basement membrane and barrier function by angiocrine factors. Nat. Commun. 8, 15374. [PubMed: 28524846]

Berry WL, and Janknecht R (2013). KDM4/JMJD2 histone demethylases: epigenetic regulators in cancer cells. Cancer Res. 73, 2936–2942. [PubMed: 23644528]

Birge RB, Boeltz S, Kumar S, Carlson J, Wanderley J, Calianese D, Barcinski M, Brekken RA, Huang X, Hutchins JT, et al. (2016). Phosphatidylserine is a global immunosuppressive signal in efferocytosis, infectious disease, and cancer. Cell Death Differ. 23, 962–978. [PubMed: 26915293]

Byrne LC, Dalkara D, Luna G, Fisher SK, Clérin E, Sahel JA, Léveillard T, and Flannery JG (2015). Viral-mediated RdCVF and RdCVFL expression protects cone and rod photoreceptors in retinal degeneration. J. Clin. Invest. 125, 105–116. [PubMed: 25415434]

Chiang CK, Tworak A, Kevany BM, Xu B, Mayne J, Ning Z, Figeys D, and Palczewski K (2017). Quantitative phosphoproteomics reveals involvement of multiple signaling pathways in early phagocytosis by the retinal pigmented epithelium. J. Biol. Chem. 292, 19826–19839. [PubMed: 28978645]

Chin RM, Fu X, Pai MY, Vergnes L, Hwang H, Deng G, Diep S, Lomenick B, Meli VS, Monsalve GC, et al. (2014). The metabolite α-ketoglutarate extends lifespan by inhibiting ATP synthase and TOR. Nature 510, 397–401. [PubMed: 24828042]

Chinchore Y, Begaj T, Wu D, Drokhlyansky E, and Cepko CL (2017). Glycolytic reliance promotes anabolism in photoreceptors. eLife 6, e25946. [PubMed: 28598329]

Chutkow WA, Patwari P, Yoshioka J, and Lee RT (2008). Thioredoxininteracting protein (Txnip) is a critical regulator of hepatic glucose production. J. Biol. Chem. 283, 2397–2406. [PubMed: 17998203]

Du J, Rountree A, Cleghorn WM, Contreras L, Lindsay KJ, Sadilek M, Gu H, Djukovic D, Raftery D, Satrústegui J, et al. (2016a). Phototransduction Influences Metabolic Flux and Nucleotide Metabolism in Mouse Retina. J. Biol. Chem. 291, 4698–4710. [PubMed: 26677218]

Du J, Yanagida A, Knight K, Engel AL, Vo AH, Jankowski C, Sadilek M, Tran VT, Manson MA, Ramakrishnan A, et al. (2016b). Reductive carboxylation is a major metabolic pathway in the retinal pigment epithelium. Proc. Natl. Acad. Sci. USA 113, 14710–14715. [PubMed: 27911769]

Fahim AT, Daiger SP, and Weleber RG (1993). Nonsyndromic Retinitis Pigmentosa Overview. In GeneReviews(R) [Internet], Pagon RA, Adam MP, Ardinger HH, Wallace SE, Amemiya A, Bean LJH, Bird TD, Ledbetter N, Mefford HC, and Smith RJH, et al., eds. (University of Washington, Seattle).

Grenell A, Wang Y, Yam M, Swarup A, Dilan TL, Hauer A, Linton JD, Philp NJ, Gregor E, Zhu S, et al. (2019). Loss of MPC1 reprograms retinal metabolism to impair visual function. Proc. Natl. Acad. Sci. USA 116, 3530–3535. [PubMed: 30808746]

Havula E, and Hietakangas V (2018). Sugar sensing by ChREBP/Mondo-Mlx-new insight into downstream regulatory networks and integration of nutrient-derived signals. Curr. Opin. Cell Biol. 51, 89–96. [PubMed: 29278834]

Hu P, and Luo BH (2013). Integrin bi-directional signaling across the plasma membrane. J. Cell. Physiol. 228, 306–312. [PubMed: 22767296]

Hue L, and Taegtmeyer H (2009). The Randle cycle revisited: a new head for an old hat. Am. J. Physiol. Endocrinol. Metab. 297, E578–E591.

Huy H, Song HY, Kim MJ, Kim WS, Kim DO, Byun JE, Lee J, Park YJ, Kim TD, Yoon SR, et al. (2018). TXNIP regulates AKT-mediated cellular senescence by direct interaction under glucose-mediated metabolic stress. Aging Cell 17, e12836. [PubMed: 30168649]

Jiang L, Shestov AA, Swain P, Yang C, Parker SJ, Wang QA, Terada LS, Adams ND, McCabe MT, Pietrak B, et al. (2016). Reductive carboxylation supports redox homeostasis during anchorage-independent growth. Nature 532, 255–258. [PubMed: 27049945]

Kanow MA, Giarmarco MM, Jankowski CS, Tsantilas K, Engel AL, Du J, Linton JD, Farnsworth CC, Sloat SR, Rountree A, et al. (2017). Biochemical adaptations of the retina and retinal pigment

epithelium support a metabolic ecosystem in the vertebrate eye. Elife 6, e28899. [PubMed: 28901286]

Kuiper JW, Pluk H, Oerlemans F, van Leeuwen FN, de Lange F, Fransen J, and Wieringa B (2008). Creatine kinase-mediated ATP supply fuels actin-based events in phagocytosis. PLoS Biol. 6, e51. [PubMed: 18336068]

Law AL, Parinot C, Chatagnon J, Gravez B, Sahel JA, Bhattacharya SS, and Nandrot EF (2015). Cleavage of Mer tyrosine kinase (MerTK) from the cell surface contributes to the regulation of retinal phagocytosis. J. Biol. Chem. 290, 4941–4952. [PubMed: 25538233]

Lemke G (2017). Phosphatidylserine Is the Signal for TAM Receptors and Their Ligands. Trends Biochem. Sci. 42, 738–748. [PubMed: 28734578]

Léveillard T, Philp NJ, and Sennlaub F (2019). Is Retinal Metabolic Dysfunction at the Center of the Pathogenesis of Age-related Macular Degeneration? Int. J. Mol. Sci. 20, E762. [PubMed: 30754662]

Lin YH, Currinn H, Pocha SM, Rothnie A, Wassmer T, and Knust E (2015). AP-2-complex-mediated endocytosis of Drosophila Crumbs regulates polarity by antagonizing Stardust. J. Cell Sci. 128, 4538–4549. [PubMed: 26527400]

Liu Y, Lu X, Huang L, Wang W, Jiang G, Dean KC, Clem B, Telang S, Jenson AB, Cuatrecasas M, et al. (2014). Different thresholds of ZEB1 are required for Ras-mediated tumour initiation and metastasis. Nat. Commun. 5, 5660. [PubMed: 25434817]

Longo N, Frigeni M, and Pasquali M (2016). Carnitine transport and fatty acid oxidation. Biochim. Biophys. Acta 1863, 2422–2435. [PubMed: 26828774]

Mackenzie RW, and Elliott BT (2014). Akt/PKB activation and insulin signaling: a novel insulin signaling pathway in the treatment of type 2 diabetes. Diabetes Metab. Syndr. Obes. 7, 55–64. [PubMed: 24611020]

Meyer AS, Zweemer AJ, and Lauffenburger DA (2015). The AXL Receptor is a Sensor of Ligand Spatial Heterogeneity. Cell Syst. 1, 25–36. [PubMed: 26236777]

Moaven H, Koike Y, Jao CC, Gurevich VV, Langen R, and Chen J (2013). Visual arrestin interaction with clathrin adaptor AP-2 regulates photoreceptor survival in the vertebrate retina. Proc. Natl. Acad. Sci. USA 110, 9463–9468. [PubMed: 23690606]

Morén H, Gesslein B, Undrén P, Andreasson S, and Malmsjö M (2011). Endovascular coiling of the ophthalmic artery in pigs to induce retinal ischemia. Invest. Ophthalmol. Vis. Sci. 52, 4880–4885. [PubMed: 21622700]

Nelson CD, Kovacs JJ, Nobles KN, Whalen EJ, and Lefkowitz RJ (2008). Beta-arrestin scaffolding of phosphatidylinositol 4-phosphate 5-kinase Ialpha promotes agonist-stimulated sequestration of the beta2-adrenergic receptor. J. Biol. Chem. 283, 21093–21101. [PubMed: 18534983]

Park KS, Xu CL, Cui X, and Tsang SH (2018). Reprogramming the metabolome rescues retinal degeneration. Cell Mol. Life Sci. 75, 1559–1566. [PubMed: 29332245]

Petit L, Ma S, Cipi J, Cheng SY, Zieger M, Hay N, and Punzo C (2018). Aerobic Glycolysis Is Essential for Normal Rod Function and Controls Secondary Cone Death in Retinitis Pigmentosa. Cell Rep. 23, 2629–2642. [PubMed: 29847794]

Punzo C, Kornacker K, and Cepko CL (2009). Stimulation of the insulin/mTOR pathway delays cone death in a mouse model of retinitis pigmentosa. Nat. Neurosci. 12, 44–52. [PubMed: 19060896]

Rasmussen KD, and Helin K (2016). Role of TET enzymes in DNA methylation, development, and cancer. Genes Dev. 30, 733–750. [PubMed: 27036965]

Ross JW, Fernandez de Castro JP, Zhao J, Samuel M, Walters E, Rios C, Bray-Ward P, Jones BW, Marc RE, Wang W, et al. (2012). Generation of an inbred miniature pig model of retinitis pigmentosa. Invest. Ophthalmol. Vis. Sci. 53, 501–507. [PubMed: 22247487]

Ruggiero L, Connor MP, Chen J, Langen R, and Finnemann SC (2012). Diurnal, localized exposure of phosphatidylserine by rod outer segment tips in wild-type but not Itgb5−/− or Mfge8−/− mouse retina. Proc. Natl. Acad. Sci. USA 109, 8145–8148. [PubMed: 22566632]

Sakami S, Maeda T, Bereta G, Okano K, Golczak M, Sumaroka A, Roman AJ, Cideciyan AV, Jacobson SG, and Palczewski K (2011). Probing mechanisms of photoreceptor degeneration in a new mouse model of the common form of autosomal dominant retinitis pigmentosa due to P23H opsin mutations. J. Biol. Chem. 286, 10551–10567. [PubMed: 21224384]

Smith TG, and Talbot NP (2010). Prolyl hydroxylases and therapeutics. Antioxid. Redox Signal. 12, 431–433. [PubMed: 19761407]

Sullivan WJ, Mullen PJ, Schmid EW, Flores A, Momcilovic M, Sharpley MS, Jelinek D, Whiteley AE, Maxwell MB, Wilde BR, et al. (2018). Extracellular Matrix Remodeling Regulates Glucose Metabolism through TXNIP Destabilization. Cell 175, 117–132. [PubMed: 30197082]

Swarup A, Samuels IS, Bell BA, Han JYS, Du J, Massenzio E, Abel ED, Boesze-Battaglia K, Peachey NS, and Philp NJ (2019). Modulating GLUT1 expression in the RPE decreases glucose levels in the retina: Impact on photoreceptors and Muller glial cells. Am. J. Physiol. Cell Physiol. 316, C121–C133. [PubMed: 30462537]

Venkatesh A, Ma S, Le YZ, Hall MN, Rüegg MA, and Punzo C (2015). Activated mTORC1 promotes long-term cone survival in retinitis pigmentosa mice. J. Clin. Invest. 125, 1446–1458. [PubMed: 25798619]

Vollrath D, Yasumura D, Benchorin G, Matthes MT, Feng W, Nguyen NM, Sedano CD, Calton MA, and LaVail MM (2015). Tyro3 Modulates Mertk-Associated Retinal Degeneration. PLoS Genet. 11, e1005723. [PubMed: 26656104]

Waldhart AN, Dykstra H, Peck AS, Boguslawski EA, Madaj ZB, Wen J, Veldkamp K, Hollowell M, Zheng B, Cantley LC, et al. (2017). Phosphorylation of TXNIP by AKT Mediates Acute Influx of Glucose in Response to Insulin. Cell Rep. 19, 2005–2013. [PubMed: 28591573]

Wang W, Fernandez de Castro J, Vukmanic E, Zhou L, Emery D, Demarco PJ, Kaplan HJ, and Dean DC (2011a). Selective rod degeneration and partial cone inactivation characterize an iodoacetic acid model of Swine retinal degeneration. Invest. Ophthalmol. Vis. Sci. 52, 7917–7923. [PubMed: 21896868]

Wang W, Noel J, Kaplan HJ, and Dean DC (2011b). Circulating reactive oxidant causes apoptosis of retinal pigment epithelium and cone photoreceptors in the mouse central retina. Ophthalmol. Eye Dis. 3, 45–54. [PubMed: 23861623]

Wang W, Zhou L, Lee SJ, Liu Y, Fernandez de Castro J, Emery D, Vukmanic E, Kaplan HJ, and Dean DC (2014). Swine cone and rod precursors arise sequentially and display sequential and transient integration and differentiation potential following transplantation. Invest. Ophthalmol. Vis. Sci. 55, 301–309. [PubMed: 24327609]

Wang W, Lee SJ, Scott PA, Lu X, Emery D, Liu Y, Ezashi T, Roberts MR, Ross JW, Kaplan HJ, and Dean DC (2016). Two-Step Reactivation of Dormant Cones in Retinitis Pigmentosa. Cell Rep. 15, 372–385. [PubMed: 27050517]

Wu N, Zheng B, Shaywitz A, Dagon Y, Tower C, Bellinger G, Shen CH, Wen J, Asara J, McGraw TE, et al. (2013). AMPK-dependent degradation of TXNIP upon energy stress leads to enhanced glucose uptake via GLUT1. Mol. Cell 49, 1167–1175. [PubMed: 23453806]

Zhang L, Du J, Justus S, Hsu CW, Bonet-Ponce L, Wu WH, Tsai YT, Wu WP, Jia Y, Duong JK, et al. (2016). Reprogramming metabolism by targeting sirtuin 6 attenuates retinal degeneration. J. Clin. Invest. 126, 4659–4673. [PubMed: 27841758]

Zhou L, Wang W, Liu Y, Fernandez de Castro J, Ezashi T, Telugu BP, Roberts RM, Kaplan HJ, and Dean DC (2011). Differentiation of induced pluripotent stem cells of swine into rod photoreceptors and their integration into the retina. Stem Cells 29, 972–980. [PubMed: 21491544]

Highlights

- Contact of rod outer segments with RPE regulates glucose transport to photoreceptors
- Outer segment mimetics restore photoreceptor glucose transport in retinitis pigmentosa

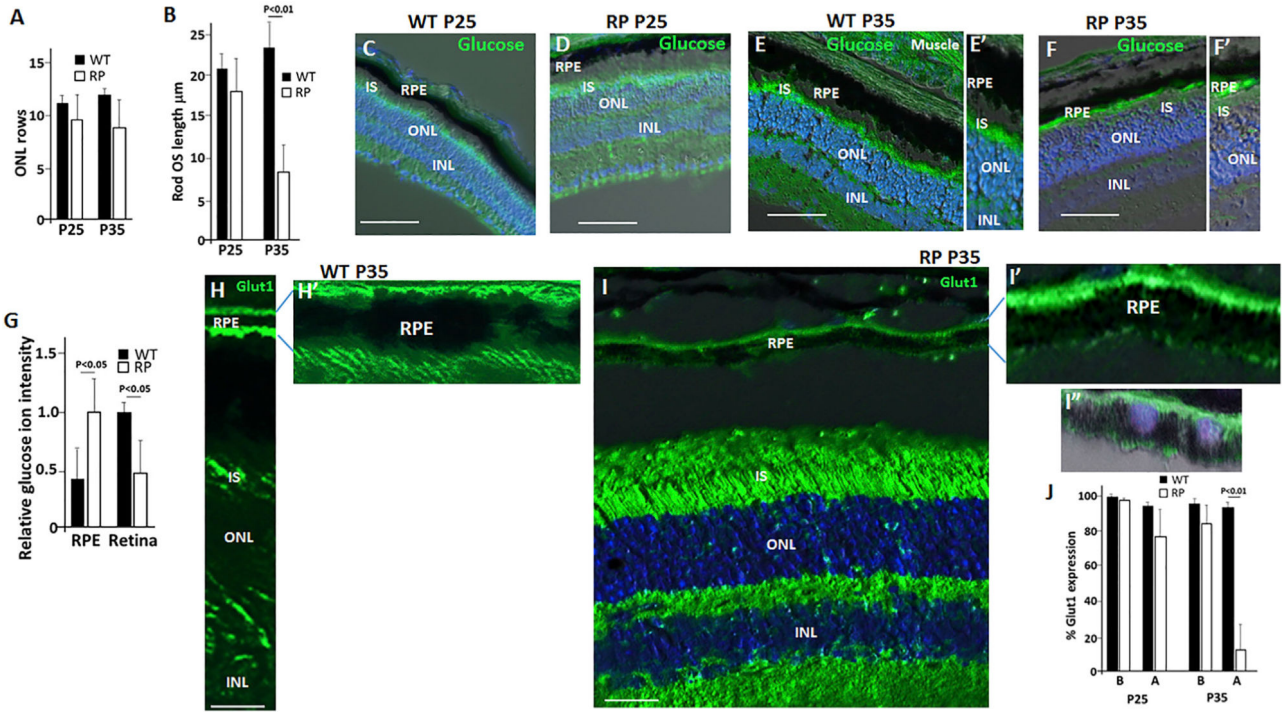

Figure 1. Diminished Glucose Transport from RPE to Photoreceptors Is Linked to ROS Length and the Pattern of RPE Glut1 Expression

(A) ONL rows were counted in a 300 µm linear section starting at the optic nerve, as described (Wang et al., 2016). See also Figure S4B.

(B) Diminished average Rho^+ ROS length occurs at P35 in RP mice. ROS length in a 300 µm linear section starting at the optic nerve was measured as described in Figure S1A.

(C–F′) RP mice (D, F, and F′) and WT littermates (C, E, and E′) were injected in the tail vein with fluorescently labeled 2-deoxyglucose at P25 before onset of ROS shortening in the RP mice, or at P35, at the onset of ROS shortening (B). Frozen sections of the retina were used to follow glucose uptake.

(G) LC/MS steady-state quantification of glucose in the RPE and retina at P40. n = 4.

(H and H′) Immunostaining showing Glut1 expressed on the apical and basal surfaces of the RPE in WT mice at P35.

(I-I′′) Glut1 expression is diminished on the RPE apical surface in RP littermates at P35. (I′′) DAPI staining demonstrating no nuclear Glut1 immunostaining. n = 8.

(J) Quantification of Glut1 expression on the basal (B) and apical (A) RPE surface as in (H)–(I′). n = 4.

Error bars in (A), (B), (G), and (J) are SD. Bars are 100 mm in (C)–(F′) and 50 µm in (H) and (I).

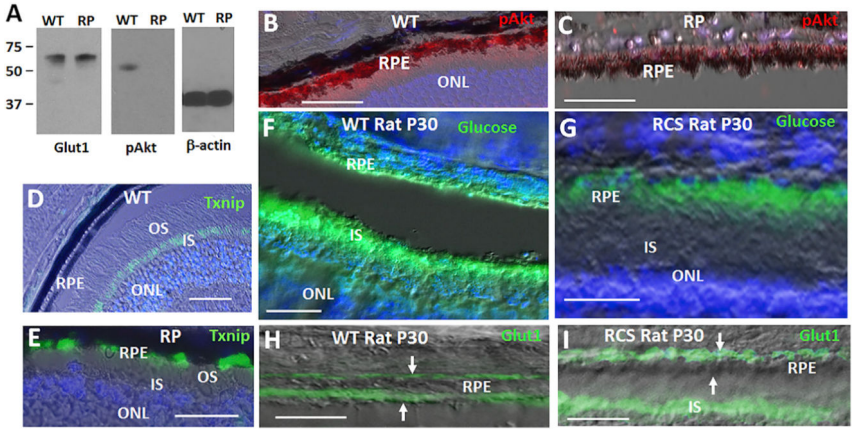

Figure 2. A Tam/pAkt/Txnip/Glut1 Pathway in RPE Glucose Transport

(A) Western blot of RPE from WT and RP mice at P40. pAkt = pAktS473.

(B and C) pAkt in RPE from WT mice (B) is diminished in the cells in RP (C). Immunostaining for Akt phosphorylated on S473 (pAktS473) is shown at P40.

(D and E) Txnip is absent in the RPE of WT mice (D), but it induced in the cells in RP (E). Txnip in photoreceptor inner segments (IS) of WT mice (D) is downregulated in IS in RP mice at P40 (E).

(F) Fluorescently labeled 2-deoxyglucose (“glucose”) transport to photoreceptor IS in WT rats at P30.

(G) Diminished transport of glucose to photoreceptors in RCS rat littermates at P30.

(H and I) Diminished Glut1 expression on the RPE apical surface in RCS rats compare to WT littermates at P30. (H) and (I) show immunostaining for Glut1. Arrows show the basal and apical surfaces of the RPE. Bars are 50 μm.

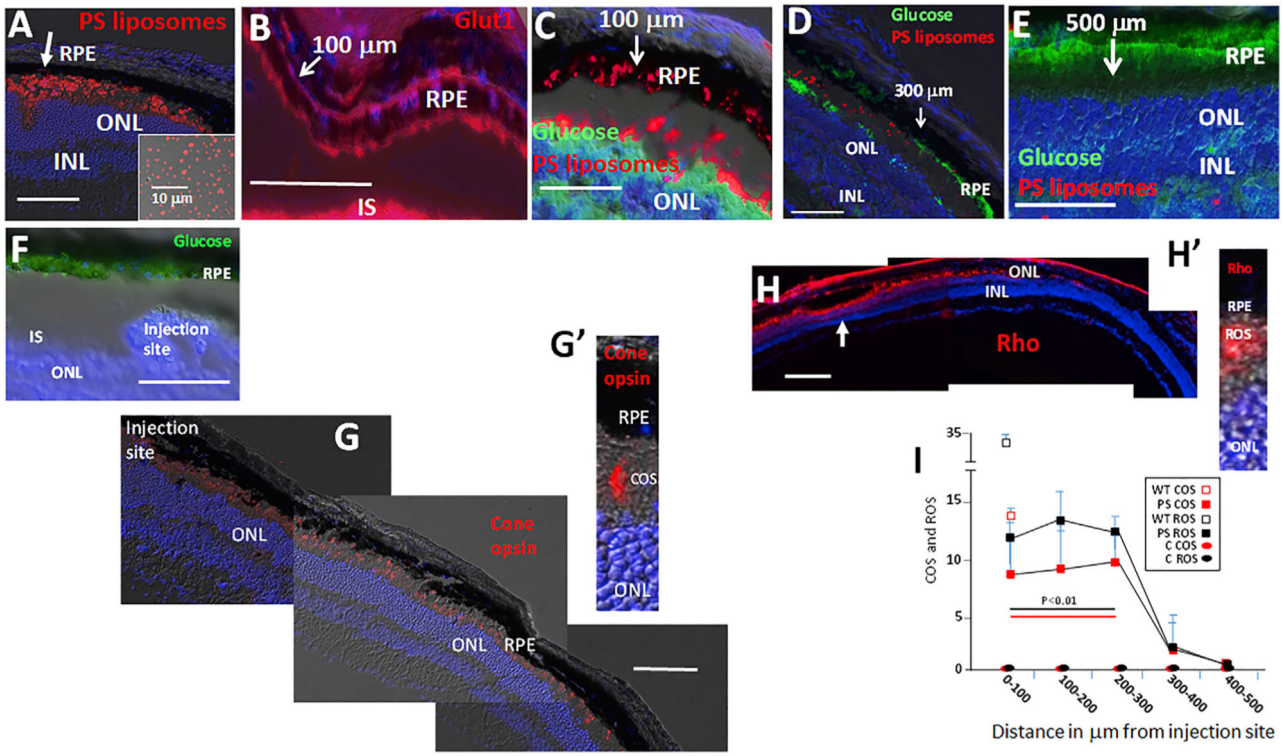

Figure 3. PS-Displaying OS Tip Mimetics Restore Apical Glut1, Glucose Transport, and Rod and Cone Photoreceptor OS in RP Mice

(A) Dye-labeled PS liposomes, shown in the inset, were injected into the subretinal space (between the RPE and ONL) of RP mice at P60. The arrow indicates the injection site. Liposome presence decreased in a gradient from the injection site at day 3.

(B) Restoration of RPE apical Glut1 expression in the region of PS liposome injection at day 3 in mice injected at P60 as in (A). Note that liposomes were not dye-labeled in this panel. The arrow shows a position 100 μm from the injection site to the left.

(C–E) Restoration of glucose transport from the RPE to photoreceptors (C–E) correlates with the PS liposome gradient and distance from the injection site at day 3 (C–E) in mice injected at P60. Arrows show indicated distance from the infection site, located to the left in the images.

(F) Injection with control liposomes does not restore glucose transport in RP mice injected at P60. Day 3 is shown.

(G and G′) Opsin^{+} COS are restored in a gradient surrounding the PS liposome injection site at day 3 in mice injected at P60. Note, liposomes were not dye-labeled in these panels. See Figure S3B for a retina flatmount showing DiI-labeled PS liposomes and cone opsin immunostaining. Side-by-side images are shown as a composite.

(H and H′) Rho^{+} ROS are restored in a gradient surrounding the PS liposome injection site (arrow) at day 3 in mice injected at P60. Note, liposomes were not dye-labeled in these panels. Side-by-side images are shown as a composite.

(I) Quantification of ROS and COS, with distance from the site of PS or control (C) liposome injection at day 3 after injection at P60. n = 7. Bars are 100 μm. Error bars are SD. See Figures S1A and S5.

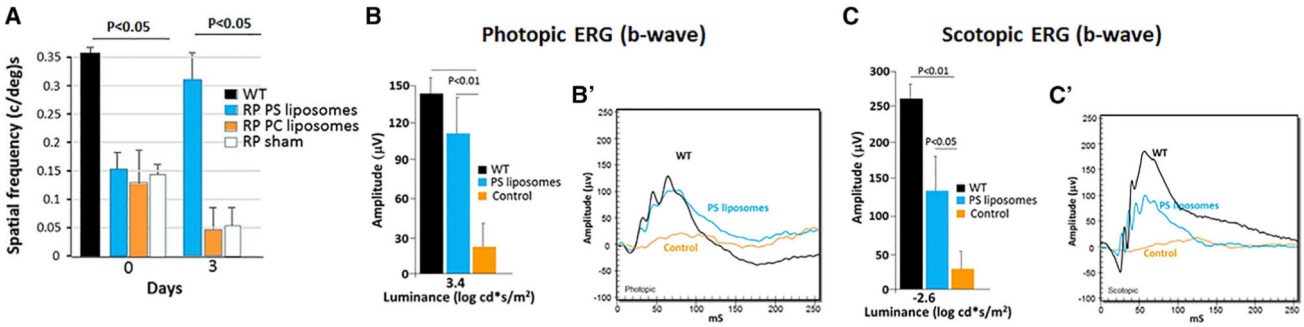

Figure 4. PS Liposome Subretinal Injection Restores Visual Acuity and Scotopic and Photopic ERG in RP Mice

(A) OKR is improved 3 days after subretinal injection of PS liposomes at P40 in RP mice. Control liposomes with PC only have no effect. n = 7.

(B) Photopic (cone) ERG b-waves are increased following PS liposome injection at P117. n = 4 (30 flashes were averaged for each eye) in (B) and (C).

(B′) Representative ERG b-waves from (B).

(C) Scotopic (rod) ERG b-waves are also increased following PS liposome injection at P117 in (B).

(C′) Representative ERG b-waves from (C). Error bars are SD.

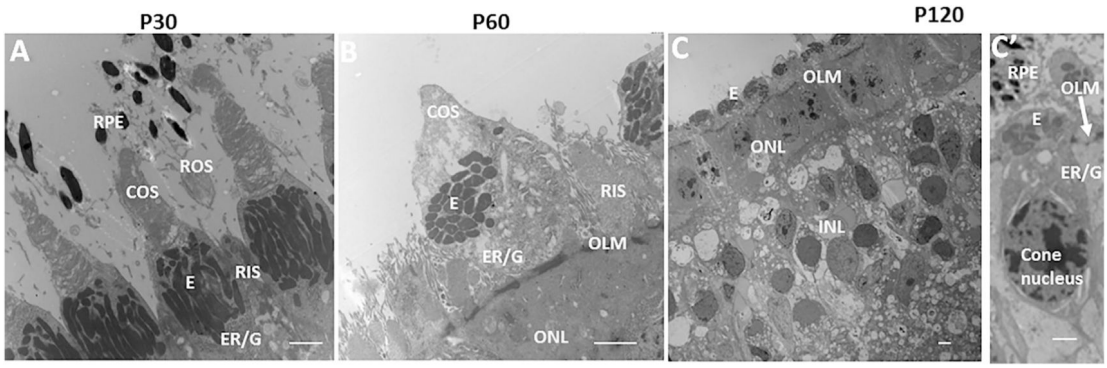

Figure 5. RP Progression in Pigs

(A–C′) EMs showing RP progression in P23H *RHO* pigs (Wang et al., 2016). At P30, ROS are shortening (A). COS are present, and cone IS contains a mitochondria-rich ellipsoid (E) with adjacent ER and golgi (G). By P60 (B), rods have diminished, with only a few RIS persisting. COS have shortened, but normal IS morphology persists. At P120 (C and C′), all rod nuclei are lost, and the ONL consists of cone nuclei (noted by their distinct elongated shape and chromatin pattern) (Wang et al., 2016). COS are lost, and the ER and G have migrated to a perinuclear position internal to the OLM, leaving the E external to the OLM. Cones persist in this dormant morphology for more than 6 years (Wang et al., 2016). RIS, rod inner segment. Bars are 5 μm. See also Figure S5.

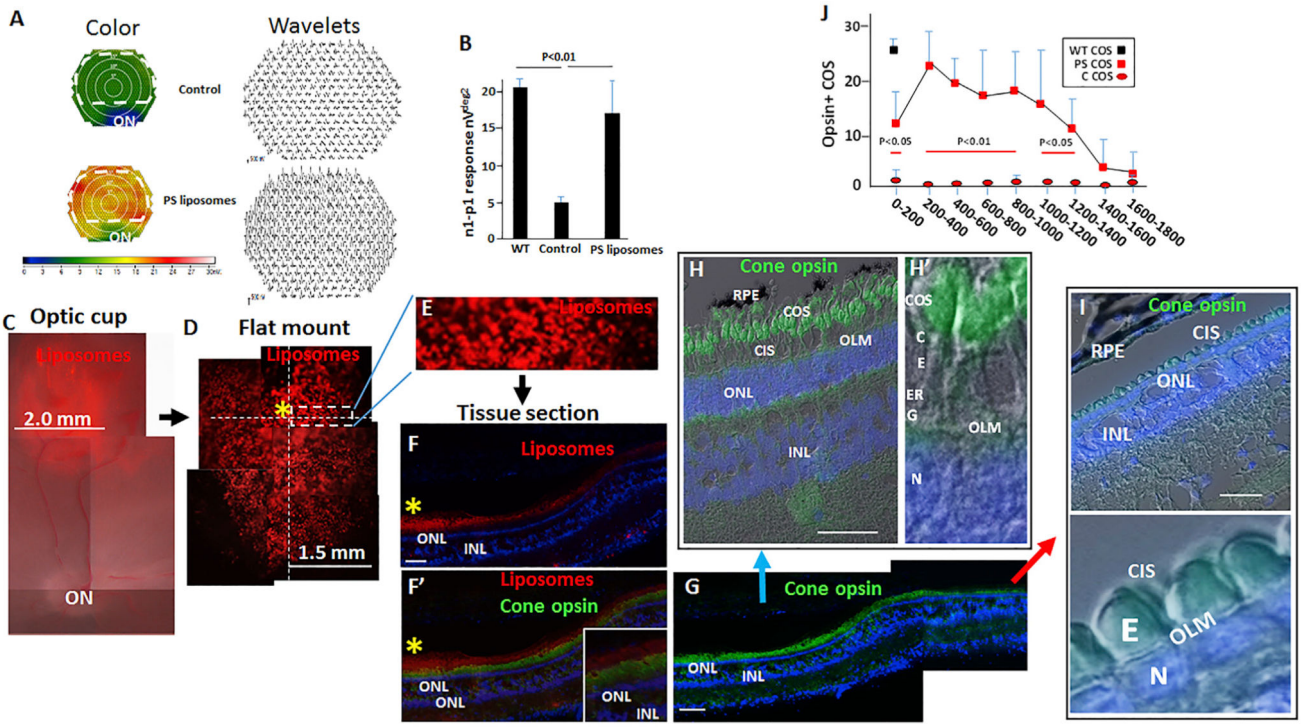

Figure 6. PS Liposome Subretinal Injection Restores Pig COS and Function in End-Stage RP

(A) Liposomes were injected subretinally in the visual streak of RP pigs at P120, and control injections were performed in the contralateral eye. mfERG is shown at injection sites in experimental and control eyes. Dashed lines show the region for quantification in (B). A color representation of wavelet height is shown on the left and wavelets themselves are shown from a complementary experiment on the right.

(B) Quantification of n1-p1 amplitude per hexagon in nV^{deg2}. Hexagons within the injection bleb (dashed line in A) were averaged.

(C) The position of a dye-labeled PS liposome bleb following subretinal injection into the visual streak above the optic nerve (ON).

(D) Retinal flat mount showing DiI-labeled PS liposomes. The yellow asterisk shows the injection site identified by serial vertical and horizontal sections through the liposome bleb (dashed lines).

(E) The boxed region from (D) is shown.

(F and F′) Sections were cut through the central region of the injection site shown in (D) and (E) and immunostained for cone opsin. See Figure S6 for a higher magnification of the injection site (yellow asterisk).

(G) The section in (F) and (F′) is shown immunostained for cone opsin, but dye-labeled liposomes are not shown in this panel so cone histology can be evaluated. Two side-by-side images are shown as a composite.

(H and H′) Higher power views of the region proximal to the injection site (blue arrow) shows restoration of COS and IS. G, golgi; E, ellipsoid; C, cilium; CIS, cone inner segments; OLM, outer limiting membrane.

(I and I′) Region distal to the injection site (red arrow) showing continued loss of COS and IS with the E, external to the OLM.

(J) Quantification of opsin^{+} COS with distance in μm from injection sites (see F–I). See Figure S5. “PS” indicates treated eyes and “C” indicates control injection (A and B). n = 6. Bars are 100 μm. Error bars are SD.

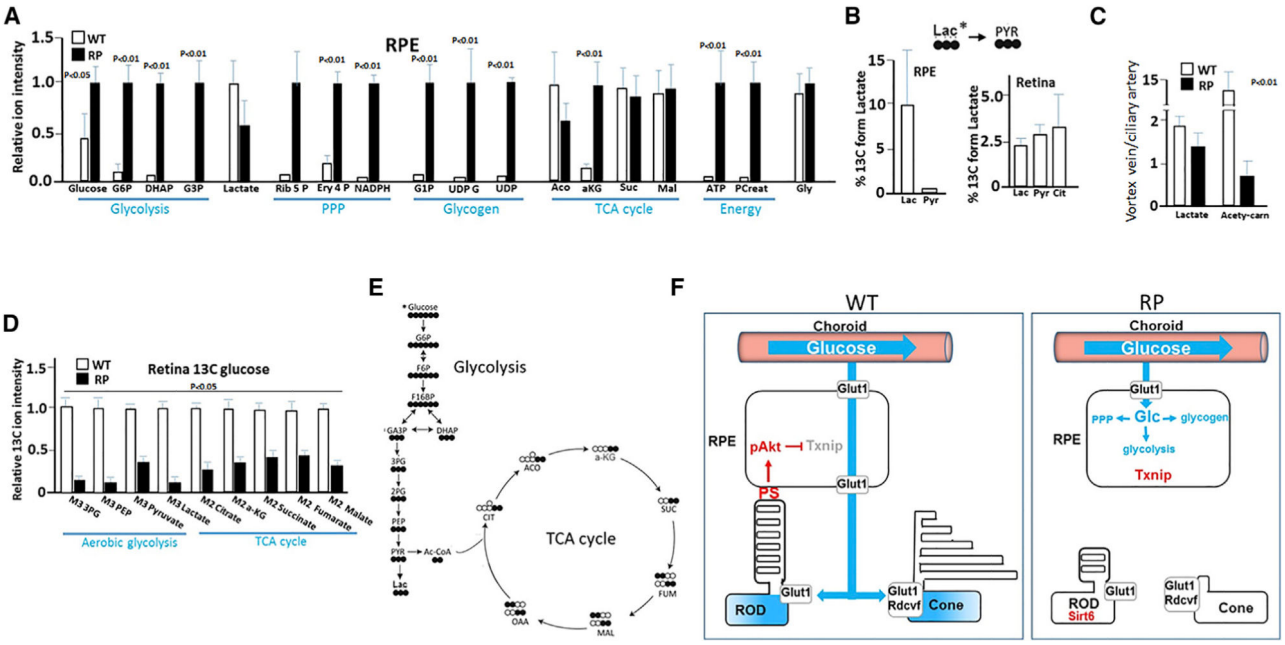

Figure 7. Onset of Glucose Metabolism in the RPE and Compromised Retinal Aerobic Glycolysis and TCA Cycle Highlight RP

(A) LC/MS of steady-state metabolites in RPE from WT and RP mice at P60. G6P, glucose-6-phosphate; DHAP, dihydroxyacetone phosphate; G3P, glucose-3-phosphate; Rib 5 P, ribulose-5-phosphate; Ery 4 P, erythose-4-phosphate; G1P, glucose-1-phosphate; UDG G, UDP glucose; Aco, aconitate; cit, citrate; α-KG, alpha-ketoglutarate; Suc, succinate; Mal, malate; Pcreat, phosphocreatine; PEP, phosphoenolpyruvate.

(B) 13C lactate (20% in 100 μL) was injected into WT mice at P60, and RPE and retina was analyzed 45 min later by GC/MS.

(C) Blood was collected from a microcatheter placed in the pig ciliary artery upstream of the RPE and downstream of the RPE in the vortex vein in an effort to evaluate secretion and uptake of metabolites by the RPE (Figures S8, S9, S10, and S11). LC/MS analysis of serum was then performed. Relative peak intensity ratios are compared for lactate and acetyl carnitine (carn) (see also Figure S11).

(D) 40% 13C glucose in 2 mL was delivered in 30 min via ciliary artery-placed microcatheter and 13C incorporation into metabolites in the retina of WT and RP pigs at P90 was examined by GC/MS.

(E) Diagram showing 13C (filled circles) glucose incorporation into glycolytic and TCA cycle intermediates.

(F) Model showing onset of glucose metabolism in the RPE and restricted transport from the RPE combine to cause glucose starvation of photoreceptors in RP, leading to loss of OS synthesis and function in both cones and rods. Error bars are SD. n = 4.

KEY RESOURCES TABLE

REAGENT or RESOURCE	SOURCE	IDENTIFIER
Antibodies		
Rhodopsin	millipore	clone 4D2; RRID:AB_10807045
anti-JH492	Jemery Nathans	N/A
anti-cone opsin	Jeremy Nathans	N/A
anti-Txnip	Abcam	ab114981; RRID:AB_10862332
Anti-Glut1	Invitrogen	MA5–31960; RRID:AB_2809254
Akt phosphorylation S473	abcam	ab81283; RRID:AB_2224551
Akt phosphorylation S308	abcam	Ab38449; RRID:AB_722678
anti- beta actin	abcam	ab8227; RRID:AB_2305186
Chemicals, Peptides, and Recombinant Proteins		
phosphytidyl serine	avantilipids	https://avantilipids.com/
phosphytidyl choline	avantilipids	https://avantilipids.com/
fluorescently labeled 2-deoxy-glucose	thermofisher	n13195
Experimental Models: Organisms/Strains		
P23H Rho mice	jackson laboratory	https://www.jax.org/strain/017628
P23H RHO pigs	Ross et al., 2012; Wang et al., 2016	N/A